

Efficient Quantum Simulation of Electron-Phonon Systems by Variational Basis State Encoder

Weitang Li,¹ Jiajun Ren,² Sainan Huai,¹ Tianqi Cai,¹ Zhigang Shuai,^{3,4,*} and Shengyu Zhang^{1,†}

¹*Tencent Quantum Lab, Tencent, Shenzhen, China*

²*College of Chemistry, Beijing Normal University, Beijing, China*

³*Department of Chemistry, Tsinghua University, Beijing, China*

⁴*School of Science and Engineering, The Chinese University of Hong Kong, Shenzhen, China*

(Dated: January 5, 2023)

Digital quantum simulation of electron-phonon systems requires truncating infinite phonon levels into N basis states and then encoding them with qubit computational basis. Unary encoding and the more compact binary/Gray encoding are the two most representative encoding schemes, which demand $\mathcal{O}(N)$ and $\mathcal{O}(\log N)$ qubits as well as $\mathcal{O}(N)$ and $\mathcal{O}(N \log N)$ quantum gates respectively. In this work, we propose a variational basis state encoding algorithm that reduces the scaling of the number of qubits and quantum gates to both $\mathcal{O}(1)$. The cost for the scaling reduction is a constant amount of additional measurement. The accuracy and efficiency of the approach are verified by both numerical simulation and realistic quantum hardware experiments. In particular, we find using 1 or 2 qubits for each phonon mode is sufficient to produce quantitatively correct results across weak and strong coupling regimes. Our approach paves the way for practical quantum simulation of electron-phonon systems on both near-term hardware and error-corrected quantum computers.

Introduction Electron-phonon couplings are pervasive in quantum materials, governing phenomena such as charge transport in semiconductors [1], vibrational spectra [2], polaron formation [3], and superconductivity [4]. Classically, expensive numerical methods such as density matrix renormalization group (DMRG) and quantum Monte-Carlo (QMC) are required to accurately simulate electron-phonon systems due to the interior many-body interaction [5–9]. Quantum computers hold promise for the simulation of quantum systems with exponential speedup over classical computers [10]. In the wake of the tremendous progress in the implementation of quantum computers [11, 12] and the dawning of the noisy intermediate-scale quantum (NISQ) era [13], how to solve electron-phonon coupling problems with quantum computers has attracted a lot of research interest [14–17].

A prominent problem for the digital quantum simulation of electron-phonon systems is how to encode the infinite phonon states with finite quantum computational basis states. The first step is usually truncating the infinite phonon states into N basis states $\{|m\rangle\}$ and then the second step is encoding $\{|m\rangle\}$ into quantum computational basis $\{|n\rangle\}$. The phonon basis states are usually the N lowest harmonic oscillator eigenstates or N uniformly distributed grid basis states. There are two established strategies to perform the encoding $\{|m\rangle\} \mapsto \{|n\rangle\}$ [18, 19]. The first is unary encoding [20, 21], in which each $|m\rangle$ is encoded to $|00\dots 1_m\dots 00\rangle$, and the total number of qubits required scales as $\mathcal{O}(N)$. The second is binary encoding, in which each $|m\rangle$ is encoded to $\prod_i \lfloor \frac{m}{2^i} \rfloor \bmod 2 \rangle$ represented by $\mathcal{O}(\log N)$ qubits [14, 15]. In terms of two-qubit gates required to simulate quantum operators such as $\hat{b}^\dagger \pm \hat{b}$ and $\hat{b}^\dagger \hat{b}$, unary encoding scales as $\mathcal{O}(N)$ and binary encoding scales as $\mathcal{O}(N \log N)$ [19]. The features of unary encoding and binary encoding are

summarized in Table 1. Compared to the simulation of electrons, the simulation of phonons consumes quantum resources in a much faster manner, which becomes the bottleneck for efficient quantum simulation of electron-phonon systems.

TABLE I. Comparison of traditional encoding schemes and the proposed variational encoding in terms of encoding formula, the number of qubits N_{qubit} required and the number of quantum gates N_{gate} required to simulate common phonon operators such as $\hat{b}^\dagger \pm \hat{b}$ and $\hat{b}^\dagger \hat{b}$.

Scheme	Formula	N_{qubit}	N_{gate}
Unary	$ m\rangle \mapsto 00\dots 1_m\dots 00\rangle$	$\mathcal{O}(N)$	$\mathcal{O}(N)$
Binary	$ m\rangle \mapsto \prod_i \lfloor \frac{m}{2^i} \rfloor \bmod 2 \rangle$	$\mathcal{O}(\log N)$	$\mathcal{O}(N \log N)$
Variational	$\sum_m C_{mn} m\rangle \mapsto n\rangle$	$\mathcal{O}(1)$	$\mathcal{O}(1)$

In this work, we propose a new basis encoding scheme called variational encoding. Variational encoding maps linear combinations of $|m\rangle$ that are most entangled to the simulated system into the computational basis, i.e. $\sum_m C_{mn} |m\rangle \mapsto |n\rangle$, where C_{mn} is determined by variational principle. The advantage of our approach is that, by encoding only the most entangled states and discarding the ones with little entanglement, the size of $\{|n\rangle\}$ can be made irrelevant to the size of $\{|m\rangle\}$. In other words, the number of qubits required scales as $\mathcal{O}(1)$. Consequently, the scaling for the number of gates is also $\mathcal{O}(1)$. Variational encoding is best suited to work in combination with variational quantum algorithms such as variational quantum eigensolver (VQE) [22, 23] and variational quantum dynamics (VQD) [24, 25]. Besides, the variational encoding is also compatible with Trotterized time evolution and quantum phase estimation (QPE) [10, 26, 27]. Numerical simulation and experiments on realistic quantum hardware based on the Hol-

stein model and spin-boson model shows that using 1 or 2 qubits for each phonon mode is typically sufficient for highly accurate results even in the strong coupling regime.

Variational Basis State Encoder Encoder coefficients C are determined by variational principle for both static and dynamic cases. We start the derivation using parameterized quantum circuit (PQC) and discuss how to incorporate the variational encoder in Trotterized time evolution and QPE later on. We use atomic units throughout the paper. More details for the derivation can be found in the Appendix.

For each phonon mode l , encoded by N_l qubits, define the variational encoder $\hat{B}[l]$

$$\hat{B}[l] = \sum_{m=1}^{2^{N_l}} \sum_{n=1}^{2^{N_l}} C[l]_{mn} |n\rangle_l \langle m| , \quad (1)$$

with orthonormal constraint $\hat{B}[l]\hat{B}[l]^\dagger = \hat{I}$. The original Hamiltonian in $|m\rangle$ basis can then be encoded to $|n\rangle$ basis $\hat{H} = \prod_l \hat{B}[l]\hat{H}\prod_l \hat{B}[l]^\dagger$. Suppose the quantum circuit is parameterized by $|\phi\rangle = \prod_k e^{i\theta_k \hat{R}_k} |\phi_0\rangle$, and then the ground state Lagrangian with multipliers $\lambda_{lnn'}$ is

$$\mathcal{L} = \langle\phi|\hat{H}|\phi\rangle + \sum_{lnn'} \lambda_{lnn'} \left(\sum_m C[l]_{mn} C[l]_{mn'} - \delta_{nn'} \right) . \quad (2)$$

Taking the derivative with respect to θ_k leads to traditional VQE with encoded Hamiltonian \hat{H} . Taking the derivative with respect to $C[l]$ and setting it to 0 yields

$$(1 - \hat{P}[l]) \langle\phi|\hat{H}'[l]|\phi\rangle = 0 , \quad (3)$$

with projector $\hat{P}[l] = \hat{B}[l]^\dagger \hat{B}[l]$ and the half encoded Hamiltonian $\hat{H}'[l] = \prod_{k \neq l} \hat{B}[k]\hat{H}\prod_k \hat{B}[k]^\dagger$. In practice, θ_k and $C[l]$ are solved iteratively until convergence. In the following, this iteration is termed macro-iteration to avoid confusion with VQE iteration.

Next, we discuss the measurement required to solve $C[l]$ from Eq. 3. Suppose the Hamiltonian can be written as $\hat{H} = \sum_x^M \hat{h}_x$ and $\hat{h}_x = \prod_k \hat{h}[k]_x$, where M is the total number of terms in the Hamiltonian and $\hat{h}[k]_x$ acts on the k th degree of freedom. The measurement of $\langle\phi|\hat{H}'[l]|\phi\rangle$ boils down to that of $\langle\phi|n\rangle_l \langle n'|\prod_{k \neq l} \hat{h}[k]_x|\phi\rangle$, where $\hat{h}[k]_x = \hat{B}[k]\hat{h}[k]_x\hat{B}[k]^\dagger$ is the encoded local operator. For electron degree of freedom a dummy encoder $\hat{B}[k] = \hat{I}$ is used for notational simplicity. The number of additional measurements for the update of $C[l]$ is thus $\mathcal{O}(2^{N_l} M)$, which is polynomial to the system size and does not increase with N . If the number of phonon modes is assumed to be linear with M and each $C[l]$ is updated independently, then the total number of measurements for all $C[l]$ is $\mathcal{O}(2^{N_l} M^2)$. The measurement overhead increases exponentially with N_l . Due to arguments presented later, N_l is usually small and does not increase

with system size. From numerical experiments, we find $N_l \leq 2$ is sufficient to produce excellent results.

For time-dependent problems, it is convenient to define $|\psi\rangle = \prod_l \hat{B}[l]^\dagger |\phi\rangle$ and use Θ_K denote both θ_k and $C[l]$. The Lagrangian with multipliers $\lambda_{lnn'}$ and $\gamma_{lnn'}$ is then

$$\begin{aligned} \mathcal{L} = & |i \sum_K \frac{\partial |\psi\rangle}{\partial \Theta_K} \dot{\Theta}_K - \hat{H} |\psi\rangle|^2 \\ & + \sum_{lnn'} \lambda_{lnn'} \operatorname{Re} \left\{ \sum_m C[l]_{mn}^* \dot{C}[l]_{mn'} \right\} \\ & + \sum_{lnn'} \gamma_{lnn'} \operatorname{Im} \left\{ \sum_m C[l]_{mn}^* \dot{C}[l]_{mn'} \right\} . \end{aligned} \quad (4)$$

The constraints ensure that $C[l]_{mn}$ remains orthonormal during time evolution. Similar to the ground state problem, the equation of motion for θ_k is the same as vanilla VQD with encoded Hamiltonian \hat{H}

$$\sum_j \operatorname{Re} \left\{ \frac{\partial \langle\phi|}{\partial \theta_k} \frac{\partial |\phi\rangle}{\partial \theta_j} \right\} \dot{\theta}_j = \operatorname{Im} \left\{ \frac{\partial \langle\phi|}{\partial \theta_k} \hat{H} |\phi\rangle \right\} . \quad (5)$$

The equation of motion for $C[l]$ reads

$$i\rho[l]\dot{C}[l]^* = (1 - \hat{P}[l]) \langle\phi|\hat{H}'[l]|\phi\rangle , \quad (6)$$

where $\rho[l]_{nn'} = \operatorname{Tr}\{\langle\phi|n\rangle \langle n'|\phi\rangle\}$ is the reduced density matrix for the N_l qubits of $|\phi\rangle$. Eq. 3 represents a $\dot{C}[l] = 0$ stationary point during real and imaginary time evolution. The measurement cost is the same as the ground state algorithm.

The VQD step described by Eq. 5 can be naturally replaced by a Suzuki-Trotter time evolution step $e^{-i\hat{H}\tau} \approx \prod_x^M e^{-i\hat{h}_x\tau}$ on a digital quantum simulator, so that Hamiltonian simulation is performed via Trotterized time evolution instead of VQD. To update $C[l]$ based on Eq. 6, measurements on the circuit should be performed for every or every several Trotter steps. The variationally encoded ground state can then be prepared by adiabatic state preparation, whose energy is accessible by QPE using \hat{H} .

It is instructive to observe that if the variational basis encoder is viewed as a wavefunction ansatz $|\psi\rangle$, then the algorithm proposed in this work can be viewed as a generalization for the local basis optimization method for DMRG [28, 29], or a special case of the recently proposed quantum-classical hybrid tensor network [30]. Thus, $\hat{B}[l]$ captures the 2^{N_l} phonon states that are most entangled with the rest of the system. For local Hamiltonian obeying the area law, the entanglement entropy between one phonon mode and the rest of the system S is a constant [31]. Consequently, $|\langle\psi|\Psi\rangle|^2$, the fidelity between the approximated encoded state and the target state has a lower bound of $\frac{2^{N_l}}{e^S}$, which lays the theoretical

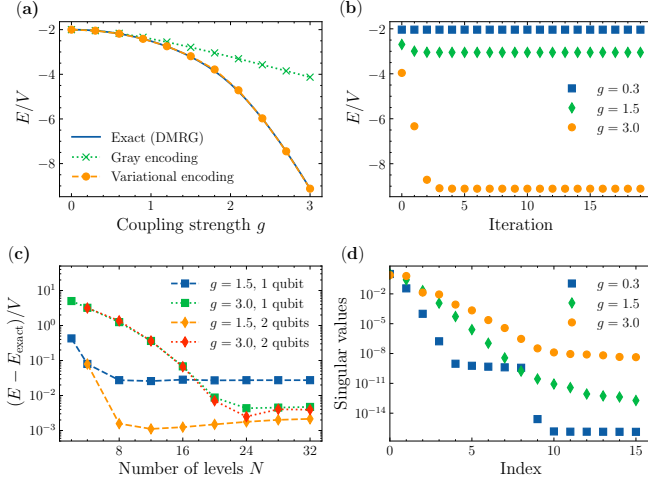


FIG. 1. Numerical simulation results for the ground state of the Holstein model. (a) Ground state energy by numerically exact DMRG, binary encoding, and variational encoding with different coupling strength g ; (b) Convergence of ground state energy with respect to the macro-iteration for variational encoding; (c) Ground state energy error for the variational encoding method at different numbers of phonon basis states N ; (d) The singular values for the Schmidt decomposition between the last phonon mode and the rest of the system.

foundation for the effectiveness of the variational encoding approach to ground state and low-lying excited state problems.

Simulations We first show numerical simulation results on a noiseless simulator and verify the algorithm on a superconducting quantum computer at the end of the section. The variational basis state encoder is first tested for VQE simulation of the one-dimensional Holstein model [32, 33]

$$\hat{H} = - \sum_{\langle i,j \rangle} V \hat{a}_i^\dagger \hat{a}_j + \sum_i \omega \hat{b}_i^\dagger \hat{b}_i + \sum_i g \omega \hat{a}_i^\dagger \hat{a}_i (\hat{b}_i^\dagger + \hat{b}_i) . \quad (7)$$

where V is the hopping coefficient, $\langle i,j \rangle$ denotes nearest neighbour pairs with periodic boundary condition, ω is the vibration frequency and g is dimensionless coupling constant. In the following, we assume $V = \omega = 1$ and adjust g for different coupling strengths. We consider a 3-site system corresponding to $3(N_l + 1)$ qubits. We use binary encoding to represent traditional encoding approaches. Unary encoding is expected to produce similar results with binary encoding only with different quantum resource budgets. The ansatz used and more details of the simulation are included in the Appendix.

We first compare the accuracy of the variational encoding and the binary encoding with $N_l = 1$. It is clear from Fig. 1(a) that variational encoding is significantly more accurate than binary encoding, especially at the strong coupling regime. Within the setup, binary encoding uses only two phonon basis states to describe each phonon mode, yet the variational encoding is allowed to use up

to 32 phonon basis states before combining them into the most entangled states. We note that the quantum circuit used for variational encoding and binary encoding is essentially the same. The number of macro-iterations to determine $C[l]$ is found to be rather small, as shown in Fig. 1(b). Fully converged results are obtained within 5 iterations. In Fig. 1(c) we show more details of the error for the variational approach. The simulation error typically decreases exponentially with respect to the number of phonon levels N included in $C[l]$. It is worth noting that quantum computational resources, including the number of qubits, the number of gates in the circuit, and the number of measurements remain constant when N is increased from 2 to 32. Furthermore, by using 2 qubits to encode each mode, it is possible to further reduce the error at the $N \rightarrow \infty$ limit. When $g = 3.0$, the error is not sensitive to N_l , which implies that the error is dominated by other sources such as limitations of the ansatz, instead of the small N_l . Fig. 1(d) shows the singular values for the Schmidt decomposition between the last phonon mode and the rest of the system by DMRG. The exponential decay ensures the fast convergence of N_l . The von Neumann entropy S for the 3 systems is found to be 0.01, 0.25, and 0.65 respectively. We also note the $g = 1.5$ case has the largest 3rd singular value, which explains why setting $N_l = 2$ significantly reduces the $g = 1.5$ error in Fig. 1(c).

We now turn to the spin-relaxation dynamics of the spin-boson model [34], described by the Hamiltonian

$$\hat{H} = \frac{\epsilon}{2} \hat{\sigma}_z + \Delta \hat{\sigma}_x + \sum_j g_j \omega_j \hat{\sigma}_z (\hat{b}_j^\dagger + \hat{b}_j) + \sum_j \omega_j \hat{b}_j^\dagger \hat{b}_j . \quad (8)$$

where ϵ is the eigenfrequency and Δ is the tunnelling rate. The coupling term has a similar form with Eq. 7 and is more commonly written as $\sum_j c_j \hat{\sigma}_z \hat{x}_j$. For systems in the condensed phase the coupling is usually characterized by the spectral density function $\mathcal{J}(\omega) = \frac{\pi}{2} \sum_j \frac{c_j^2}{\omega_j} \delta(\omega - \omega_k)$. In the following we assume $\epsilon = 0$ and $\Delta = 1$. We first use VQD for the simulation and discuss Trotterized time evolution at last. The variational Hamiltonian ansatz [35] with 3 layers is used if not otherwise specified.

The performance of variational encoding and binary encoding is first compared based on a 1-mode spin-boson model at the strong coupling ($\omega = 1$ and $g = 3$) regime, shown in Fig. 2(a). Variational encoding with $N_l = 1$ generates much more accurate dynamics than binary encoding with fewer qubits and quantum gates. The simulation of binary encoding with $N_l > 4$ is prohibited by the deep circuit depth in the ansatz. The variational encoding scheme is exceptionally efficient for this 1-mode model because Schmidt decomposition guarantees that 2 variational bases for the phonon mode are sufficient to exactly represent the system. In Fig. 2(b) a 2-mode model with $\omega_j = \frac{1}{2}, 1$ and $g_j = \frac{1}{2}, 1$ is used. Variational encoding with $N_l = 1$ is accurate at $t < 2$ but as the entan-

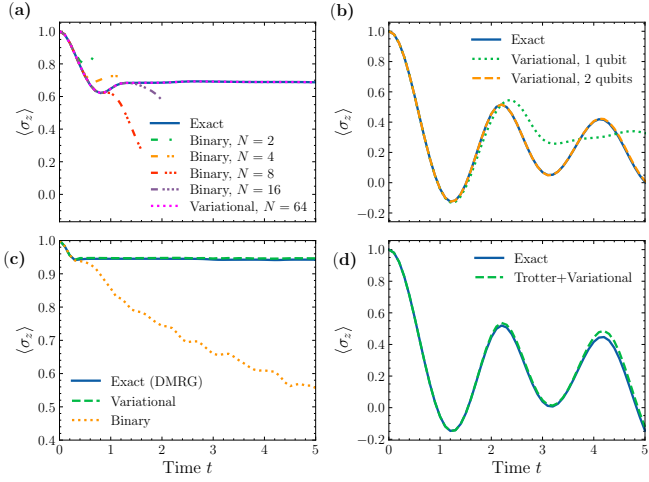


FIG. 2. Numerical simulation results for the spin-relaxation dynamics of the spin-boson model. (a) Comparison between binary encoding with different numbers of phonon basis states and variational encoding for a 1-mode spin-boson model; (b) Variational encoding with different numbers of encoding qubits N_l for a 2-mode spin-boson model; (c) Comparison between binary encoding and variational encoding for an 8-mode spin-boson model with sub-Ohmic spectral density; (d) Trotterized time evolution with variational encoding based on a 1-mode spin-boson model.

lement builds up the dynamics deviate from the exact solution. Increasing N_l to 2 effectively eliminates the error. Next, we move on to a more challenging model with 8 modes, in which ω and g are determined by discretizing a sub-Ohmic spectral density $\mathcal{J}(\omega) = \frac{\pi}{2} \alpha \omega^s \omega_c^{1-s} e^{-\omega/\omega_c}$ following the prescription in the literature [36]. The parameters are $s = \frac{1}{4}$, $\omega_c = 4$ and $\alpha = 10$. As illustrated in Fig. 2(c) variational encoding with $N_l = 1$ captures the localization behavior yet binary encoding with $N_l = 1$ completely fails. The number of layers in the variational Hamiltonian ansatz is 8 and 32 for variational and binary encoding respectively. Fig. 2(d) demonstrates the possibility to incorporate variational basis state encoder into Trotterized time evolution with $\omega = g = 1$ and $N_l = 1$. The measurement and the evolution of $C[l]$ are performed at each Trotter step.

Lastly, we verify the accuracy and efficiency of the variational encoder approach on a superconducting quantum computer. We consider the ground state problem of a 2-site Holstein model described by Eq. 7 with $g = 3$ and $N_l = 1$. The two electronic sites are represented by 1 qubit and the total number of qubits for the system is thus 3. The quantum circuit for the simulation is depicted in Fig. 3(a). The electronic degree of freedom is mapped to the second qubit, and the two phonon modes are mapped to the first and the third qubits respectively. There is one parameter to be determined by VQE in the circuit and the same ansatz is used for both binary encoding and variational encoding. More simulation details

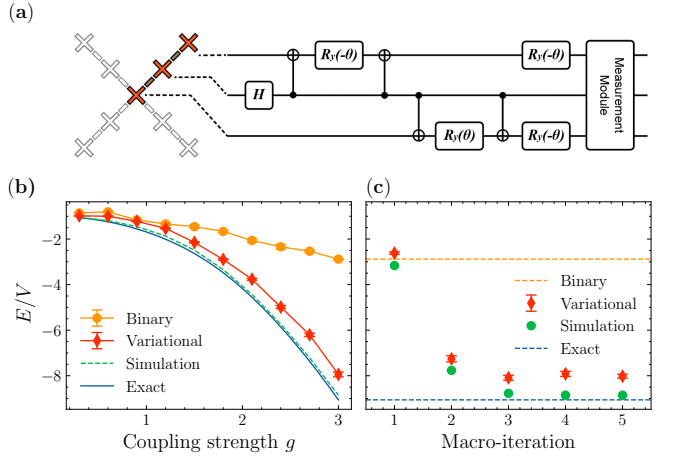


FIG. 3. Quantum hardware experiments for the ground state energy of the Holstein model with variational basis state encoder. (a) 3 qubits out of 9 qubits of a superconducting quantum computer and a one-parameter circuit are used for the simulation; (b) Ground state energy by binary encoding and variational encoding; (c) Convergence of ground state energy with respect to the macro-iteration for variational encoding.

can be found in the Appendix. In Fig. 3(b) we show the ground state energy by variational encoding from weak to strong coupling, in analog to Fig. 1(a). The simulator result is based on the parameterized quantum circuit described in Fig. 3(a) without considering gate noise and measurement uncertainty. The results in Fig. 3(b) are consistent with that in Fig. 1(a). The residual error is dominated by the intrinsic gate noise in the quantum computer. In Fig. 3(c) we show the convergence with respect to the macro-iteration for variational encoding. The algorithm is resilient to the presence of quantum noise and measurement uncertainty. The convergent energy is reached within 5 iterations.

Conclusion We proposed variational basis state encoder to encode phonon basis states into quantum computational states for efficient quantum simulation of electron-phonon systems. The proposed variational encoding approach requires only $\mathcal{O}(1)$ qubits and $\mathcal{O}(1)$ quantum gates, which is significantly better than traditional encoding schemes. The algorithm enables quantum simulation of electron-phonon systems with smaller quantum processors and shallower circuits. The additional measurement required to implement the approach is found to be also $\mathcal{O}(1)$ with respect to the number of phonon basis states and it scales quadratically with the number of Pauli strings in the Hamiltonian. The accuracy of the approach is ensured by the finite entanglement entropy between one phonon mode and the rest of the system in common electron-phonon systems. Variational basis state encoder most naturally works with variational quantum algorithms and is compatible with Trotterized time evolution, adiabatic state preparation,

and QPE. Numerical simulation and quantum hardware experiments based on VQE of the Holstein model and dynamics of the spin-boson model indicates that variational encoding is more accurate and resource-efficient than traditional encoding methods. In particular, using 1 or 2 qubits to represent each phonon mode is sufficient for accurate simulation even at the strong coupling regime where $N = 64$ phonon basis states are involved. The approach could also be extended to other quantum simulation problems involving an infinite or large local Hilbert space.

We thank Jinzhao Sun and Shixin Zhang for helpful discussions. This work is supported by the National Natural Science Foundation of China through grand numbers 22273005 and 21788102. This work is also supported by Shenzhen Science and Technology Program.

* zgshuai@tsinghua.edu.cn

† shengyzhang@tencent.com

- [1] J. Bardeen and W. Shockley, Deformation potentials and mobilities in non-polar crystals, *Phys. Rev.* **80**, 72 (1950).
- [2] M. Cardona and M. L. W. Thewalt, Isotope effects on the optical spectra of semiconductors, *Rev. Mod. Phys.* **77**, 1173 (2005).
- [3] M. B. Salamon and M. Jaime, The physics of manganites: Structure and transport, *Rev. Mod. Phys.* **73**, 583 (2001).
- [4] W. E. Pickett, Electronic structure of the high-temperature oxide superconductors, *Rev. Mod. Phys.* **61**, 433 (1989).
- [5] E. Jeckelmann and S. R. White, Density-matrix renormalization-group study of the polaron problem in the Holstein model, *Phys. Rev. B* **57**, 6376 (1998).
- [6] E. A. Nowadnick, S. Johnston, B. Moritz, R. T. Scalettar, and T. P. Devereaux, Competition between antiferromagnetic and charge-density-wave order in the half-filled Hubbard-Holstein model, *Phys. Rev. Lett.* **109**, 246404 (2012).
- [7] A. S. Mishchenko, N. Nagaosa, G. De Filippis, A. de Candia, and V. Cataudella, Mobility of Holstein polaron at finite temperature: An unbiased approach, *Phys. Rev. Lett.* **114**, 146401 (2015).
- [8] X. Cai, Z.-X. Li, and H. Yao, Antiferromagnetism induced by bond Su-Schrieffer-Heeger electron-phonon coupling: A quantum Monte Carlo study, *Phys. Rev. Lett.* **127**, 247203 (2021).
- [9] W. Li, J. Ren, and Z. Shuai, A general charge transport picture for organic semiconductors with nonlocal electron-phonon couplings, *Nat. Commun.* **12**, 4260 (2021).
- [10] S. Lloyd, Universal quantum simulators, *Science* **273**, 1073 (1996).
- [11] F. Arute, K. Arya, R. Babbush, D. Bacon, J. C. Bardin, R. Barends, R. Biswas, S. Boixo, F. G. Brandao, D. A. Buell, *et al.*, Quantum supremacy using a programmable superconducting processor, *Nature* **574**, 505 (2019).
- [12] S. Xu, Z.-Z. Sun, K. Wang, L. Xiang, Z. Bao, Z. Zhu, F. Shen, Z. Song, P. Zhang, W. Ren, *et al.*, Digital simulation of non-abelian anyons with 68 programmable superconducting qubits, arXiv preprint arXiv:2211.09802 (2022).
- [13] J. Preskill, Quantum Computing in the NISQ era and beyond, *Quantum* **2**, 79 (2018).
- [14] A. Macridin, P. Spentzouris, J. Amundson, and R. Harnik, Electron-phonon systems on a universal quantum computer, *Phys. Rev. Lett.* **121**, 110504 (2018).
- [15] P. J. Ollitrault, G. Mazzola, and I. Tavernelli, Nonadiabatic molecular quantum dynamics with quantum computers, *Phys. Rev. Lett.* **125**, 260511 (2020).
- [16] C.-K. Lee, C.-Y. Hsieh, S. Zhang, and L. Shi, Variational quantum simulation of chemical dynamics with quantum computers, *J. Chem. Theory and Comput.* **18**, 2105 (2022).
- [17] Y. Wang, J. Ren, W. Li, and Z. Shuai, Hybrid quantum-classical boson sampling algorithm for molecular vibrationally resolved electronic spectroscopy with Duschinsky rotation and anharmonicity, *J. Phys. Chem. Lett.* **13**, 6391 (2022).
- [18] N. P. Sawaya, T. Menke, T. H. Kyaw, S. Johri, A. Aspuru-Guzik, and G. G. Guerreschi, Resource-efficient digital quantum simulation of d -level systems for photonic, vibrational, and spin- s hamiltonians, *npj Quantum Inf.* **6**, 1 (2020).
- [19] O. Di Matteo, A. McCoy, P. Gysbers, T. Miyagi, R. Woloshyn, and P. Navrátil, Improving Hamiltonian encodings with the Gray code, *Phys. Rev. A* **103**, 042405 (2021).
- [20] R. Somma, G. Ortiz, E. Knill, and J. Gubernatis, Quantum simulations of physics problems, *Int. J. Quantum Inf.* **1**, 189 (2003).
- [21] A. Miessen, P. J. Ollitrault, and I. Tavernelli, Quantum algorithms for quantum dynamics: a performance study on the spin-boson model, *Phys. Rev. Res.* **3**, 043212 (2021).
- [22] A. Peruzzo, J. McClean, P. Shadbolt, M.-H. Yung, X.-Q. Zhou, P. J. Love, A. Aspuru-Guzik, and J. L. O'Brien, A variational eigenvalue solver on a photonic quantum processor, *Nat. Commun.* **5**, 1 (2014).
- [23] J. R. McClean, J. Romero, R. Babbush, and A. Aspuru-Guzik, The theory of variational hybrid quantum-classical algorithms, *New J. Physics* **18**, 023023 (2016).
- [24] Y. Li and S. C. Benjamin, Efficient variational quantum simulator incorporating active error minimization, *Phys. Rev. X* **7**, 021050 (2017).
- [25] X. Yuan, S. Endo, Q. Zhao, Y. Li, and S. C. Benjamin, Theory of variational quantum simulation, *Quantum* **3**, 191 (2019).
- [26] D. S. Abrams and S. Lloyd, Quantum algorithm providing exponential speed increase for finding eigenvalues and eigenvectors, *Phys. Rev. Lett.* **83**, 5162 (1999).
- [27] A. Aspuru-Guzik, A. D. Dutoi, P. J. Love, and M. Head-Gordon, Simulated quantum computation of molecular energies, *Science* **309**, 1704 (2005).
- [28] C. Zhang, E. Jeckelmann, and S. R. White, Density matrix approach to local Hilbert space reduction, *Phys. Rev. Lett.* **80**, 2661 (1998).
- [29] C. Guo, A. Weichselbaum, J. von Delft, and M. Vojta, Critical and strong-coupling phases in one-and two-bath spin-boson models, *Phys. Rev. Lett.* **108**, 160401 (2012).
- [30] X. Yuan, J. Sun, J. Liu, Q. Zhao, and Y. Zhou, Quantum simulation with hybrid tensor networks, *Phys. Rev. Lett.* **127**, 040501 (2021).
- [31] J. Eisert, M. Cramer, and M. B. Plenio, Colloquium:

Area laws for the entanglement entropy, Rev. Mod. Phys. **82**, 277 (2010).

[32] T. Holstein, Studies of polaron motion: Part I. the molecular-crystal model, Ann. Phys. **8**, 325 (1959).

[33] T. Holstein, Studies of polaron motion: Part II. the “small” polaron, Ann. Phys. **8**, 343 (1959).

[34] A. J. Leggett, S. Chakravarty, A. T. Dorsey, M. P. Fisher, A. Garg, and W. Zwerger, Dynamics of the dissipative two-state system, Rev. Mod. Phys. **59**, 1 (1987).

[35] D. Wecker, M. B. Hastings, and M. Troyer, Progress towards practical quantum variational algorithms, Phys. Rev. A **92**, 042303 (2015).

[36] H. Wang and M. Thoss, From coherent motion to localization: II. dynamics of the spin-boson model with sub-Ohmic spectral density at zero temperature, Chem. Phys. **370**, 78 (2010).

[37] S.-X. Zhang, J. Allcock, Z.-Q. Wan, S. Liu, J. Sun, H. Yu, X.-H. Yang, J. Qiu, Z. Ye, Y.-Q. Chen, *et al.*, Tensorcircuit: a quantum software framework for the nisq era, arXiv preprint arXiv:2205.10091 (2022).

[38] J. Ren, W. Li, T. Jiang, Y. Wang, and Z. Shuai, The RENORMALIZER package. <https://github.com/shuaigroup/renormalizer> (2021).

[39] P. Virtanen, R. Gommers, T. E. Oliphant, M. Haberland, T. Reddy, D. Cournapeau, E. Burovski, P. Peterson, W. Weckesser, J. Bright, S. J. van der Walt, M. Brett, J. Wilson, K. J. Millman, N. Mayorov, A. R. J. Nelson, E. Jones, R. Kern, E. Larson, C. J. Carey, I. Polat, Y. Feng, E. W. Moore, J. VanderPlas, D. Laxalde, J. Perktold, R. Cimrman, I. Henriksen, E. A. Quintero, C. R. Harris, A. M. Archibald, A. H. Ribeiro, F. Pedregosa, P. van Mulbregt, and SciPy 1.0 Contributors, SciPy 1.0: Fundamental Algorithms for Scientific Computing in Python, Nat. Methods **17**, 261 (2020).

I. Derivation of variational basis state encoder

Time-independent equation

We start with the Lagrangian defined in the main text, i.e. Eq. 2. Taking the derivative with respect to $C[l]_{mn}$ and setting it to 0 yields

$$\langle \phi | n \rangle_l \langle m | \hat{H}'[l] | \phi \rangle + \sum_{n'} \lambda_{lnn'} C[l]_{mn'} = 0 . \quad (9)$$

Multiply with $C[l]_{mn''}$

$$\sum_m C[l]_{mn''} \langle \phi | n \rangle_l \langle m | \hat{H}'[l] | \phi \rangle + \sum_{n'} \lambda_{lnn'} \sum_m C[l]_{mn'} C[l]_{mn''} = 0 , \quad (10)$$

and use the $C[l]$ orthonormal condition $\sum_m C[l]_{mn} C[l]_{mn'} = \delta_{nn'}$ to get λ

$$\lambda_{lnn'} = - \sum_m C[l]_{mn'} \langle \phi | n \rangle_l \langle m | \hat{H}'[l] | \phi \rangle . \quad (11)$$

Substitute λ into Eq. 9 yields

$$\langle \phi | n \rangle_l \langle m | \hat{H}'[l] | \phi \rangle - \sum_{n'm} C[l]_{mn'} \langle \phi | n \rangle_l \langle m | \hat{H}'[l] | \phi \rangle C[l]_{m'n'} = 0 . \quad (12)$$

Using

$$\hat{P} = \hat{B}[l]^\dagger B[l] = \sum_{mm'} \sum_n |m\rangle_l C[l]_{mn} C[l]_{m'n} \langle m' | , \quad (13)$$

to simplify the notation of the second term

$$\langle \phi | n \rangle_l \langle m | \hat{H}'[l] | \phi \rangle - \langle \phi | n \rangle_l \langle m | \hat{P} \hat{H}'[l] | \phi \rangle = 0 . \quad (14)$$

Rearranging and rewriting in matrix form, we get the equation for $C[l]$

$$(1 - \hat{P}[l]) \langle \phi | \hat{H}'[l] | \phi \rangle = 0 . \quad (15)$$

Quantum circuit measurement

In this section, we discuss the quantum circuit measurement required to solve $C[l]$ from Eq. 3. The key quantity to be computed is matrix $G[l]_{mn}$, defined as

$$G[l]_{mn} = \langle \phi | n \rangle_{l-1} \langle m | \hat{H}'[l] | \phi \rangle . \quad (16)$$

Express \hat{H} in sum-of-product form $\hat{H} = \sum_x^M \prod_k \hat{h}[k]_x$, using notations in the main text, and we get

$$\begin{aligned} G[l]_{mn} &= \sum_x^M \langle \phi | n \rangle_{l-1} \langle m | \prod_{k \neq l} \hat{B}[k] \prod_k \hat{h}[k]_x \prod_k \hat{B}[k]^\dagger | \phi \rangle \\ &= \sum_x^M \langle \phi | n \rangle_{l-1} \langle m | \hat{h}[l]_x \hat{B}[l]^\dagger \prod_{k \neq l} \hat{h}[k]_x | \phi \rangle . \end{aligned} \quad (17)$$

Here we assume $\prod_{k \neq l} \hat{h}[k]_x$ can be expressed by a constant amount of Pauli strings. Represent $\hat{h}[l]_x$ in operator form

$$\hat{h}[l]_x = \sum_{mm'} h[l]_{xm'm} |m'\rangle_{l-1} \langle m| . \quad (18)$$

$G[l]_{mn}$ then becomes

$$G[l]_{mn} = \sum_x^M \sum_{m'n'} h[l]_{xm'm} C[l]_{m'n'} \langle \phi | n \rangle_{l-1} \langle n' | \prod_{k \neq l} \hat{h}[k]_x | \phi \rangle . \quad (19)$$

Thus to evaluate $G[l]_{mn}$ it is sufficient to measure $\langle \phi | n \rangle_{l-1} \langle n' | \prod_{k \neq l} \hat{h}[k]_x | \phi \rangle$. $|n\rangle_{l-1} \langle n'|$ in general is not Hermitian, and the real and imaginary parts can be measured by

$$\begin{aligned} \text{Re} \left\{ \langle \phi | n \rangle_{l-1} \langle n' | \prod_{k \neq l} \hat{h}[k]_x | \phi \rangle \right\} &= \frac{1}{2} \langle \phi | (|n\rangle_{l-1} \langle n'| + |n'\rangle_{l-1} \langle n|) \prod_{k \neq l} \hat{h}[k]_x | \phi \rangle , \\ \text{Im} \left\{ \langle \phi | n \rangle_{l-1} \langle n' | \prod_{k \neq l} \hat{h}[k]_x | \phi \rangle \right\} &= \frac{1}{2} \langle \phi | i(|n'\rangle_{l-1} \langle n| - |n\rangle_{l-1} \langle n'|) \prod_{k \neq l} \hat{h}[k]_x | \phi \rangle . \end{aligned} \quad (20)$$

To evaluate all matrix elements in $G[l]$, the total number of measurements required scales as $\mathcal{O}(2^{N_l} M)$.

Time-dependent equation

In this section, we derive the time-dependent equation for $C[l]$. For time-dependent problems, $C[l]$ in general is complex

$$C[l] = D[l] - iE[l] , \quad (21)$$

where both $D[l]$ and $E[l]$ are real. The minus sign is for convenience expressing $\hat{B}^\dagger | \phi \rangle$. From the definition we have

$$\frac{\partial |\psi\rangle}{\partial E[l]_{mn}} = i \frac{\partial |\psi\rangle}{\partial D[l]_{mn}} . \quad (22)$$

The starting point is the Lagrangian Eq. 4 defined in the main text. Taking the derivative with respect to $\dot{\Theta}_K$

yields

$$\begin{aligned}
\frac{\partial \mathcal{L}}{\partial \dot{\Theta}_K} &= \sum_J \frac{\partial \langle \psi |}{\partial \Theta_J} \frac{\partial | \psi \rangle}{\partial \Theta_K} \dot{\Theta}_J + \sum_J \frac{\partial \langle \psi |}{\partial \Theta_K} \frac{\partial | \psi \rangle}{\partial \Theta_J} \dot{\Theta}_J \\
&\quad + i \frac{\partial \langle \psi |}{\partial \Theta_K} \hat{H} | \psi \rangle - i \langle \psi | \hat{H} \frac{\partial | \psi \rangle}{\partial \Theta_K} \\
&\quad + \sum_{l n n'} \lambda_{l n n'} \operatorname{Re} \left\{ \sum_m C[l]_{m n}^* \frac{\partial \dot{C}[l]_{m n'}}{\partial \dot{\Theta}_K} \right\} \\
&\quad + \sum_{l n n'} \gamma_{l n n'} \operatorname{Im} \left\{ \sum_m C[l]_{m n}^* \frac{\partial \dot{C}[l]_{m n'}}{\partial \dot{\Theta}_K} \right\} .
\end{aligned} \tag{23}$$

We first consider the case of $\Theta_K = \theta_k$, and then

$$\begin{aligned}
\frac{\partial \mathcal{L}}{\partial \dot{\theta}_k} &= \sum_J \frac{\partial \langle \psi |}{\partial \Theta_J} \frac{\partial | \psi \rangle}{\partial \theta_k} \dot{\Theta}_J + \sum_J \frac{\partial \langle \psi |}{\partial \theta_k} \frac{\partial | \psi \rangle}{\partial \Theta_J} \dot{\Theta}_J \\
&\quad + i \frac{\partial \langle \psi |}{\partial \theta_k} \hat{H} | \psi \rangle - i \langle \psi | \hat{H} \frac{\partial | \psi \rangle}{\partial \theta_k} \\
&= 2 \sum_J \operatorname{Re} \left\{ \frac{\partial \langle \psi |}{\partial \theta_k} \frac{\partial | \psi \rangle}{\partial \Theta_J} \right\} \dot{\Theta}_J - 2 \operatorname{Im} \left\{ \frac{\partial \langle \psi |}{\partial \theta_k} \hat{H} | \psi \rangle \right\} ,
\end{aligned} \tag{24}$$

which means at the $\frac{\partial \mathcal{L}}{\partial \dot{\theta}_k} = 0$ minimum, we have

$$\sum_J \operatorname{Re} \left\{ \frac{\partial \langle \psi |}{\partial \theta_k} \frac{\partial | \psi \rangle}{\partial \Theta_J} \right\} \dot{\Theta}_J = \operatorname{Im} \left\{ \frac{\partial \langle \psi |}{\partial \theta_k} \hat{H} | \psi \rangle \right\} . \tag{25}$$

Substitute Θ_J with θ_k , $D[l]_{m n}$ and $E[l]_{m n}$

$$\begin{aligned}
\sum_J \operatorname{Re} \left\{ \frac{\partial \langle \psi |}{\partial \theta_k} \frac{\partial | \psi \rangle}{\partial \Theta_J} \right\} \dot{\Theta}_J &= \sum_j \operatorname{Re} \left\{ \frac{\partial \langle \psi |}{\partial \theta_k} \frac{\partial | \psi \rangle}{\partial \theta_j} \right\} \dot{\theta}_j \\
&\quad + \sum_{l m n} \operatorname{Re} \left\{ \frac{\partial \langle \psi |}{\partial \theta_k} \frac{\partial | \psi \rangle}{\partial D[l]_{m n}} \right\} \dot{D}[l]_{m n} \\
&\quad + \sum_{l m n} \operatorname{Re} \left\{ \frac{\partial \langle \psi |}{\partial \theta_k} \frac{\partial | \psi \rangle}{\partial E[l]_{m n}} \right\} \dot{E}[l]_{m n} .
\end{aligned} \tag{26}$$

Using Eq. 22 the last two terms become

$$\sum_{l m n} \operatorname{Re} \left\{ \frac{\partial \langle \psi |}{\partial \theta_k} \frac{\partial | \psi \rangle}{\partial D[l]_{m n}} \right\} \dot{D}[l]_{m n} + \sum_{l m n} \operatorname{Re} \left\{ \frac{\partial \langle \psi |}{\partial \theta_k} \frac{\partial | \psi \rangle}{\partial E[l]_{m n}} \right\} \dot{E}[l]_{m n} = \sum_{l m n} \operatorname{Re} \left\{ \frac{\partial \langle \psi |}{\partial \theta_k} \frac{\partial | \psi \rangle}{\partial D[l]_{m n}} \dot{C}[l]_{m n}^* \right\} , \tag{27}$$

which is zero because

$$\sum_{m n} \frac{\partial \langle \psi |}{\partial \theta_k} \frac{\partial | \psi \rangle}{\partial D[l]_{m n}} \dot{C}[l]_{m n}^* = \sum_{m n} \frac{\partial \langle \phi |}{\partial \theta_k} \hat{B}[l] | m \rangle_l \langle n | \dot{C}[l]_{m n}^* | \phi \rangle = 0 , \tag{28}$$

where the constraint $\sum_m C[l]_{m n} \dot{C}[l]_{m n}^* = 0$ is used. Thus the simplified equation of motion reads

$$\sum_j \operatorname{Re} \left\{ \frac{\partial \langle \psi |}{\partial \theta_k} \frac{\partial | \psi \rangle}{\partial \theta_j} \right\} \dot{\theta}_j = \operatorname{Im} \left\{ \frac{\partial \langle \psi |}{\partial \theta_k} \hat{H} | \psi \rangle \right\} , \tag{29}$$

or equivalently

$$\sum_j \operatorname{Re} \left\{ \frac{\partial \langle \phi |}{\partial \theta_k} \frac{\partial | \phi \rangle}{\partial \theta_j} \right\} \dot{\theta}_j = \operatorname{Im} \left\{ \frac{\partial \langle \phi |}{\partial \theta_k} \hat{H} | \phi \rangle \right\} . \tag{30}$$

In short, the equation of motion for θ_k is the same as vanilla VQD with encoded Hamiltonian \hat{H} .

Next we consider the case of $\Theta_K = D[l]$ and $\Theta_K = E[l]$. After some complex algebra, we have

$$i \sum_J \frac{\partial \langle \psi |}{\partial D[l]_{mn}} \frac{\partial |\psi \rangle}{\partial \Theta_J} \dot{\Theta}_J + i \frac{1}{2} \sum_{n'} \lambda_{ln'n} C[l]_{mn'}^* - \frac{1}{2} \sum_{n'} \gamma_{ln'n} C[l]_{mn'}^* = \frac{\partial \langle \psi |}{\partial D[l]_{mn}} \hat{H} |\psi \rangle . \quad (31)$$

Similar to the case of $\Theta_K = \theta_k$, substitute Θ_J with θ_k , $D[l]_{mn}$ and $E[l]_{mn}$

$$\begin{aligned} \sum_J \frac{\partial \langle \psi |}{\partial D[l]_{mn}} \frac{\partial |\psi \rangle}{\partial \Theta_J} \dot{\Theta}_J &= \sum_k \frac{\partial \langle \psi |}{\partial D[l]_{mn}} \frac{\partial |\psi \rangle}{\partial \theta_k} \dot{\theta}_k + \sum_{km'n'} \frac{\partial \langle \psi |}{\partial D[l]_{mn}} \frac{\partial |\psi \rangle}{\partial D[k]_{m'n'}} \dot{C}[k]_{m'n'}^* \\ &= \sum_k \frac{\partial \langle \psi |}{\partial D[l]_{mn}} \frac{\partial |\psi \rangle}{\partial \theta_k} \dot{\theta}_k + \sum_{n'} \frac{\partial \langle \psi |}{\partial D[l]_{mn}} \frac{\partial |\psi \rangle}{\partial D[l]_{mn'}} \dot{C}[l]_{mn'}^* . \end{aligned} \quad (32)$$

Here the orthonormal condition is again used. Substitute the equation back into Eq. 31.

$$i \sum_k \frac{\partial \langle \psi |}{\partial D[l]_{mn}} \frac{\partial |\psi \rangle}{\partial \theta_k} \dot{\theta}_k + i \sum_{n'} \frac{\partial \langle \psi |}{\partial D[l]_{mn}} \frac{\partial |\psi \rangle}{\partial D[l]_{mn'}} \dot{C}[l]_{mn'}^* + \frac{1}{2} \sum_{n'} (i\lambda_{ln'n} - \gamma_{ln'n}) C[l]_{mn'}^* = \frac{\partial \langle \psi |}{\partial D[l]_{mn}} \hat{H} |\psi \rangle , \quad (33)$$

Following the same strategy with the derivation of the time-independent equation, multiply Eq. 33 with $C[l]_{mn}$

$$i \sum_k \langle \phi | n \rangle_l \langle l | n' | \frac{\partial |\phi \rangle}{\partial \theta_k} \dot{\theta}_k + \frac{1}{2} (i\lambda_{ln'n} - \gamma_{ln'n}) = \sum_m C[l]_{mn'} \frac{\partial \langle \psi |}{\partial D[l]_{mn}} \hat{H} |\psi \rangle , \quad (34)$$

where $\sum_m C[l]_{mn'}^* C[l]_{mn} = \delta_{n'n}$ and $\sum_m \dot{C}[l]_{mn'}^* C[l]_{mn} = 0$ are used. Then, multiply again with $C[l]_{mn}^*$

$$i \sum_k \frac{\partial \langle \psi |}{\partial D[l]_{mn}} \frac{\partial |\psi \rangle}{\partial \theta_k} \dot{\theta}_k + \frac{1}{2} \sum_{n'} (i\lambda_{ln'n} - \gamma_{ln'n}) C[l]_{mn'}^* = \hat{P}[l] \frac{\partial \langle \psi |}{\partial D[l]_{mn}} \hat{H} |\psi \rangle . \quad (35)$$

Use this equation to eliminate λ and γ in Eq. 33, we get the equation of motion for $C[l]$

$$i \sum_{n'} \frac{\partial \langle \psi |}{\partial D[l]_{mn}} \frac{\partial |\psi \rangle}{\partial D[l]_{mn'}} \dot{C}[l]_{mn'}^* = (1 - \hat{P}[l]) \frac{\partial \langle \psi |}{\partial D[l]_{mn}} \hat{H} |\psi \rangle , \quad (36)$$

which can be simplified to Eq. 6. The measurement required for time evolution is in the same order as the static VQE algorithm.

In the end, we note that imaginary time evolution might be another approach to finding the ground state, in addition to the iterative method described in the main text. Imaginary time evolution might also be a feasible approach to determine $C[l]$ as an alternative to solving Eq. 3.

II. Numerical noiseless simulations

All numerical quantum circuit simulation is performed using the TENSORCIRCUIT [37] package without considering noise. Classical DMRG simulation is performed using the RENORMALIZER package [38]. We use harmonic oscillator eigenstates for phonon basis states. Using positional states might affect the performance of traditional encodings because of the truncation, however, we expect variational encoding to be insensitive to the choice of phonon basis states at the $N \rightarrow \infty$ limit. We use Gray code for binary encoding as an improvement to the standard approach [18]. For both ground state simulation and dynamics simulation, $C[l]$ is initialized as $C[l]_{mn} = \delta_{mn}$.

For the VQE simulation of the Holstein model, the following ansatz is used

$$|\phi\rangle = \prod_l^L \left\{ \prod_{(j,k)} e^{\theta_{ljk} (\hat{a}_j^\dagger \hat{a}_k - \hat{a}_k^\dagger \hat{a}_j)} \prod_j e^{\theta_{lj} \hat{a}_j^\dagger \hat{a}_j (\hat{b}_j^\dagger - \hat{b}_j)} \right\} |\phi_0\rangle . \quad (37)$$

where L is the number of layers and $L = 3$ is adopted. The advantage of Eq. 37 is enforcing real-valued wavefunction. The circuit parameters $\vec{\theta}$ are optimized by the L-BFGS-G method implemented in SCIPY package [39]. The parameter gradient is calculated by auto-differentiation. The initial values for the parameters are set to zero at the first round

of the macro-iteration. In subsequent macro-iterations, the previously optimized parameters are used as the initial value for faster convergence. Eq. 3 is solved by the DF-SANE method implemented in SciPY [39]. Since this is a non-linear equation, we provide 3 initial guesses and adopt the one with the lowest energy. The solved $C[l]$ sometimes does not satisfy the orthonormal condition due to numerical imprecision and the orthonormal condition is enforced by QR decomposition in each macro-iteration.

For the VQD simulation of the spin-boson model, the variational Hamiltonian ansatz used is more complex than the VQE simulation. Because $C[l]$ is complex, $\hat{B}[l]\hat{h}[l]_x\hat{B}[l]^\dagger$ spans the whole Hermitian matrix space. Thus for $\hat{h}[l]_x$ the whole Pauli matrix set $\{X, Y, Z, I\}^{\otimes N_l}$ is added to the ansatz. To obtain the quantities required to calculate θ_k , the Jacobian of the wavefunction $\phi(\vec{\theta})$ is firstly calculated by auto-differentiation, and then the r.h.s and l.h.s of Eq. 5 is calculated by matrix multiplication. How to measure the quantities in realistic quantum circuits is well described in the literature [16]. To calculate $\hat{C}[l]$ it is necessary to take the inverse of $\rho[l]$ which is sometimes ill-conditioned. We add 1×10^{-5} to the diagonal elements of $\rho[l]$ for regularization. The time evolution of θ_k and $C[l]$ is carried out using the RK45 method implemented in SciPY [39]. We observe that the gradient of θ_k is usually much larger than $C[l]$. Thus it is possible to evolve the two sets of parameters separately, which deserves further investigation. For Trotterized time evolution, $N = 16$ and a time step of 0.01 are used.

III. Experiments on a superconducting quantum processor

Device parameters

The superconducting quantum processor, as shown in Fig. 3(a), is composed of nine computational transmon qubits with each pair of neighboring qubits mediated via a tunable coupler, forming a cross-shaped architecture. Each computational qubit has an independent readout cavity for state measurement and XY/Z control lines for state operation. High-fidelity simultaneous single-shot readout for all qubits are achieved with the help of the multistage amplification with the Josephson parametric amplifier (JPA) functioning as the first stage of the amplification. The fundamental device parameters including qubit parameters and gate parameters are outlined in Table. II and Table. III, where the parasitic ZZ interaction between qubits is suppressed by the coupler.

TABLE II. Single qubit gate parameters. ω_r is the resonant frequency of the readout cavity for each qubit. $\omega_{j,max}$ ($j = 1 \sim 9$) are the maximum resonant frequencies when qubits are biased at the sweet spot. $\omega_{j,idle}$ ($j = 1 \sim 9$) are the idle frequencies for implementing the single-qubit operations. α_j ($j = 1 \sim 9$) are the qubits' anharmonicities. T_1 , $T_{2,idle}$ and $T_{2E,idle}$ are the corresponding energy relaxation time, Ramsey dephasing time and echoed dephasing time for the qubits measured at the idle frequency. The readout fidelities are typically characterized by detecting each qubit in $|g\rangle$ ($|e\rangle$) when it is prepared in $|g\rangle$ ($|e\rangle$), labeled by $F_{0,j}$ and $F_{1,j}$. To mitigate the error coming from the readout infidelity, the outcomes are reconstructed with the calibration matrix through the Bayes' rule. Single-qubit errors e_{sq} are measured with randomized benchmarking (RB).

	Q_0	Q_1	Q_2	Q_3	Q_4	Q_5	Q_6	Q_7	Q_8
ω_r (GHz)	6.874	6.825	6.931	6.901	6.845	6.786	6.991	6.961	6.806
$\omega_{j,max}$ (GHz)	4.003	4.215	4.479	4.689	4.470	4.479	4.657	4.512	4.362
$\omega_{j,idle}$ (GHz)	3.988	4.187	4.464	4.668	4.404	4.359	4.641	4.498	4.223
$\alpha_j/2\pi$ (MHz)	-260	-258	-255	-250	-254	-258	-253	-257	-264
T_1 (μ s)	35.3	31.6	29.5	27.7	33.9	34.3	33.3	22.1	31.8
$T_{2,idle}$ (μ s)	11.0	10.2	32.6	38.2	9.1	5.6	43.1	24.1	4.3
$T_{2E,idle}$ (μ s)	48.2	38.4	47.8	44.2	31.6	21.8	56.8	32.9	18.6
$F_{0,j}$ (%)	96.9	97.4	98.6	98.9	98.7	98.4	96.3	97.2	94.1
$F_{1,j}$ (%)	93.7	94.3	92.5	94.3	94.5	94.6	92.7	92.4	90.9
e_{sq} (%)	0.07	0.32	0.06	0.07	0.08	0.05	0.06	0.15	0.08

Experimental details

We use 3 qubits out of the 9-qubit computer for the 2-site Holstein model

$$\hat{H} = -V(a_1^\dagger a_2 + a_2^\dagger a_1) + \omega b_1^\dagger b_1 + \omega b_2^\dagger b_2 + g\omega a_1^\dagger a_1(b_1^\dagger + b_1) + g\omega a_2^\dagger a_2(b_2^\dagger + b_2). \quad (38)$$

The electronic degree of freedom is mapped to the second qubit. Thus, $a_1^\dagger a_1$ is mapped to $\frac{1}{2}(1 + Z_1)$ and $a_2^\dagger a_2$ is mapped to $\frac{1}{2}(1 - Z_1)$. The phonon modes are mapped to the first and the third qubit. With binary encoding and

TABLE III. Two qubits gate parameters. $\omega_{c,idle}$ are the idle frequencies for each coupler where the ZZ interaction between neighboring computational qubits are maximally suppressed. ξ_{ZZ} is the residual ZZ interaction between each qubit pairs. Two-qubit gates are implemented with the controlled-Z (CZ) and the corresponding gate errors $e_{tq,CZ}$ are characterized with RB.

	$Q_0 - Q_1$	$Q_0 - Q_2$	$Q_0 - Q_3$	$Q_0 - Q_4$	$Q_1 - Q_5$	$Q_2 - Q_6$	$Q_3 - Q_7$	$Q_4 - Q_8$
$\omega_{c,idle}$ (GHz)	5.020	5.445	5.570	5.335	5.325	5.595	5.695	5.355
$ \xi_{ZZ} $ (kHz)	18.0	10.0	5.0	8.0	2.0	3.0	5.0	2.0
$e_{tq,CZ}$ (%)	1.57	2.22	1.99	2.47	0.91	1.04	1.2	0.96

$N_l = 1$, the Hamiltonian in the Pauli string form reads

$$\hat{H} = -VX_1 + \frac{1}{2}\omega(1 - Z_0) + \frac{1}{2}\omega(1 - Z_2) + \frac{1}{2}g\omega(1 + Z_1)X_0 + \frac{1}{2}g\omega(1 - Z_1)X_2 . \quad (39)$$

For variational encoding, we assume $C[l] = C$. That is, the two modes share the same variational encoder. This is a reasonable assumption for translational invariant systems. Supposing $\hat{b}^\dagger\hat{b}$ and $\hat{b}^\dagger + \hat{b}$ are mapped to the following form

$$\begin{aligned} \hat{B}(\hat{b}^\dagger\hat{b})\hat{B}^\dagger &= c_{1i}I + c_{1x}X + c_{1z}Z \\ \hat{B}(\hat{b}^\dagger + \hat{b})\hat{B}^\dagger &= c_{2i}I + c_{2x}X + c_{2z}Z , \end{aligned} \quad (40)$$

the encoded Hamiltonian is then

$$\begin{aligned} \hat{H} &= -VX_1 + \omega(c_{1i}I_0 + c_{1x}X_0 + c_{1z}Z_0) + \omega(c_{1i}I_2 + c_{1x}X_2 + c_{1z}Z_2) \\ &+ \frac{1}{2}g\omega(1 + Z_1)(c_{2i}I_0 + c_{2x}X_0 + c_{2z}Z_0) + \frac{1}{2}g\omega(1 - Z_1)(c_{2i}I_2 + c_{2x}X_2 + c_{2z}Z_2) . \end{aligned} \quad (41)$$

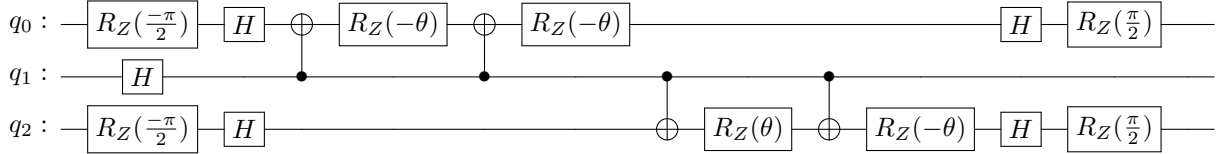
We use the following ansatz for the parameterized quantum circuit

$$|\phi\rangle = \prod_{j=1}^2 e^{\theta_j a_j^\dagger a_j (b_j^\dagger - b_j)} \frac{1}{\sqrt{2}} (|000\rangle + |100\rangle) , \quad (42)$$

Because $C[1] = C[2]$, the parameter space can be further simplified by setting $\theta_1 = \theta_2$. With binary encoding, the ansatz transforms to

$$|\phi\rangle = e^{i\theta Y_2} e^{-i\theta Z_1 Y_2} e^{i\theta Y_0} e^{i\theta Z_1 Y_0} H_1 |0\rangle . \quad (43)$$

The ansatz is compiled into the following quantum circuit with 4 CNOT gates.



Each energy term is measured by 8192 shots, and the uncertainty is obtained by repeating the measurement 5 times and taking the standard deviation. For the update of $C[l]$, 4096 shots are performed for each term. Local readout error mitigation is applied for all results presented unless otherwise stated.

In Fig. 4 we plot the energy landscape $E(\theta)/V$ in VQE with binary encoding. Both raw data and data with local readout error mitigation (EM) are presented for the energy expectation from quantum hardware. The mitigated landscape is in decent agreement with the perfect simulator. A minimum at around $\theta = 0.6$ is clearly visible. We note that the perfect simulator is also based on the $N_l = 1$ ansatz and N is far smaller than what is physically demanded. Thus the minimum presented by the perfect simulator can not be recognized as the ground truth.

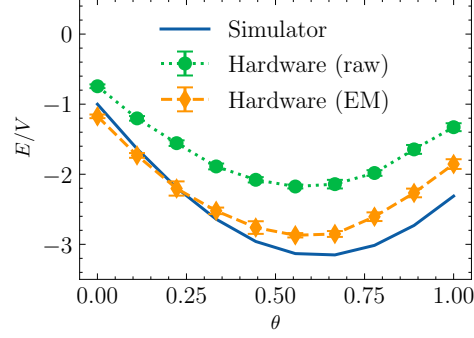


FIG. 4. VQE energy landscape for the 2-site Holstein model with binary encoding. For the data from quantum hardware, both raw data and data with readout error mitigation are presented. The error bar indicates the measurement uncertainty.